Engineering Structures 321 (2024) 119022

Contents lists available at ScienceDirect

Engineering Structures

journal homepage: www.elsevier.com/locate/engstruct

# Experimental study on progressive collapse behavior of frame structures triggered by impact column removal

Fan Yi *, Wei-Jian Yi, Jing-Ming Sun, Yun Zhou, Wang-Xi Zhang, Qing-Feng He

*College of Civil Engineering, Hunan Provincial Key Lab on Damage Diagnosis for Engineering Structures, Hunan University, Changsha 410082, China*

ARTICLE INFO

*Keywords:*
Progressive collapse
Event-dependent
Impact loading
Impact column removal
Reinforced concrete frame structures
Experimental study

ABSTRACT

In the research field investigating the progressive collapse of building structures, event-dependent collapse processes have gained increasing attention in analytical and numerical studies. Different events could cause varying effects on progressive collapse resistance. The alternate load path could be related to events that could also lead to variations in load actions. However, experimental studies on reinforced concrete (RC) frame structures triggering structural column removal by the low-velocity impact have not been reported. Therefore, this paper performed an initial experimental study employing impact loading as the extreme event to investigate subsequent progressive collapse behavior of structures. Tests were conducted on six RC substructures consisting of a two-span beam and a structural column. Gravity loads were applied to the top of substructures, and a pendulum impact setup was utilized to remove RC columns by low-velocity impact. When the column underwent lateral failures, the downward force exerted by longitudinal steel bars of the column, before they fractured, pulled the two-span beam beyond the compressive arch action (CAA) stage, leading to a collapse process entirely different from their event-independent counterparts. The parametric study based on experimental results indicated that low-elevation impact and increase of column longitudinal bars detrimentally affected the performance of two-span beams resisting progressive collapse, while the increase in concrete strength partially improved the residual bearing capacity after impact column removal (ICR). Based on a dynamic model, a simplified calculation method is proposed for quantifying the downward force.

## 1. Introduction

Progressive collapse, also known as disproportionate collapse, refers to the complete or partial collapse of a building structure that is disproportionate to the initial local damage in terms of severity or area [1]. Tragedies like the World Trade Center collapse and the Champlain Towers South apartment collapse indicate that the influence of low-probability-high-consequence (LPHC) events on structural safety needs to be rigorously considered. Although some conceptual design principles [2] or specific design methods and criteria [3,4] resisting progressive collapse have been proposed in certain standards, they mostly adopt the event-independent assumption, emphasizing the significance of alternate load path while commonly neglecting the influence of events on the alternate load path and on the load itself. This can lead to a potential overestimation on structural resistance, as has been confirmed in studies concerning explosion [5–8] or fire [9,10] accidents. RC frame structures, as an extensively adopted structural form, have drawn considerable attention regarding their safety issues in both academic and industrial communities. Therefore, it is imperative to obtain comprehensive and accurate understanding on the progressive collapse resistance of RC frame structures under various event-dependent conditions.

In terms of event-dependent studies, Gombeda et al. proposed an analysis framework for mapping blast-induced damage to building structures [7]. Kiakojouri et al. developed the alternate path method by incorporating influencing parameters like column removal time and damage level to consider the blast effects [8]. Stewart investigated the spatial variability of blast loads and its damage and collapse risks on RC buildings [11]. Yu et al. performed tests on RC substructures with columns removed by contact detonations [12]. Shi et al. proposed a damage assessment method for RC frame structures considering close-in explosions [13]. As one of the extreme loads that is regarded as the possible trigger event of progressive collapse [1], impact loading received relatively less attention. Kang and Kim [14] simulated scenarios where heavy trucks impacted steel frames. The simulation results suggested that structures could collapse when the impact velocity exceeds 80

* Corresponding author.
*E-mail address:* yifance@hnu.edu.cn (F. Yi).

https://doi.org/10.1016/j.engstruct.2024.119022
Received 4 July 2024; Received in revised form 24 August 2024; Accepted 18 September 2024

km/h. Janfada et al. [15] also investigated the influence of impact velocity and mass on progressive collapse responses of steel frames by numerical simulations. Although a consensus has been reached regarding the higher risks of progressive collapse under event-dependent scenarios, existing research still does not address some critical issues. For example, at the physical mechanism level, there is a lack of explanation for the aftermath of various identified threats on the progressive collapse resistance of RC structures. Furthermore, more systematic experimental studies need to be conducted, especially those removing columns by impact loading. In some papers, hydrogen gas cannons [16] or pendulums [17,18] were employed to trigger the sudden column removal. However, these studies were still event-independent because the removed columns were temporary supports rather than structural columns that monolithically poured and connected with superstructures by longitudinal bars. A recent study found that longitudinal bars in columns subjected to explosive loading could generate transient tensile strains that might affect the demolition results [19]. Inspired by this phenomenon, some other researchers realized that removed RC columns in explosion events might exert a downward force affecting the result of progressive collapse, so they conducted related drop-weight impact tests [20]. In a preliminary investigation [21], a viewpoint was proposed that impact column removal (ICR) could develop a downward force and weaken the progressive collapse resistance of RC frame structures. The investigation results suggested that the process of ICR could be divided into the impact loading stage and gravity loading stage. Above all, it becomes evident that extreme loads triggering column removal could lead to remarkable adverse effects on the progressive collapse performance of structures. However, the recognition of this issue, along with related computational theories, still needs compelling supports like experimental evidence.

The impact response studies on RC columns, especially those with experiments, provide guidance for seizing the progressive collapse under ICR and for conducting experiments. Sharma et al. established a performance-based evaluation framework for shear demand and capacity assessments of RC columns under impact loading [22]. Li et al. [23] reported that constant axial loads have positive effects on RC columns resisting impact loading when lateral deformation is insignificant. Utilizing the lever principle, Sun et al. [24] applied constant axial loads in impact tests. It is found that failure modes under impact loading shift from flexural to shear with the increase of axial load ratios and impact velocity. Based on impact tests, Gurbuz et al. [25] realized and mentioned higher progressive collapse risks for structures suffering impact loading, but further investigation was not conducted. It is noteworthy that axial loads are typically applied by hydraulic actuators [26,27], disk springs [23, 28–30], or gravity loads [24] in impact tests of RC columns because structural responses under axial compression are principal concerns. All existing lateral impact experiments on RC columns only considered the limited stiffness characteristics of the top end of columns.

The substructural test is the main experimental method for RC structures to investigate the progressive collapse behavior. Yi et al. [31] performed a static experimental study on a planar substructure to investigate mechanisms resisting progressive collapse on RC frame structures. Su et al. [32] constructed two-span-beam substructures with axial restraints in static tests to study the effects of CAA. Qian and Li [33] evaluated the influence of membrane actions on RC structures by beam-slab substructures. By dynamic beam-column substructures, Qian and Li [34] also suggested that measured dynamic load increase factors are significantly less than values recommended in a relevant design code [3]. Given the trade-off between experimental costs and the reliability of results, this study also employed substructural tests.

Considering the preceding discussions, this paper engineered a pendulum impact setup to perform an experimental study on RC frame substructures subjected to ICR. After dynamic column removal tests, static tests were performed on remaining specimens because residual load-bearing capacity could be of assessment for evaluating progressive collapse resistance under different column removal methods and could provide instructions for relevant rescue and retrofitting issues [35]. Furthermore, utilizing single-degree-freedom (SDOF) dynamic models, the composition of the downward force and its simplified calculation method are proposed to provide ideas for event-dependent progressive collapse research and design.

## 2. Experimental program

### 2.1. Specimen design and material parameters

The prototype structure was designed based on *Code for design of concrete structures (GB50010–2010)* in China and scaled down with a 1/3 ratio for substructures. The prototype structure had span lengths of 5400 mm and 6000 mm in the x and y directions, respectively. The floor height was 5400 mm for the first floor and 3300 mm for the remaining floors. The columns had cross-sectional dimensions of 500 × 500 mm$^2$, while the beams measured 400 × 600 mm$^2$. The substructures were designed in a T-shaped configuration consisting of an RC column and two RC beams intersected at the middle joint, and were subjected to boundary restraints, both lateral and rotational, provided by stubs anchored on steel corbels, as illustrated in Fig. 1. The longitudinal bars of the RC column extended 360 mm into the foundation and included a 280 mm hooked tail portion to ensure reliable anchorage within the surrounding concrete. The foundation was secured by eight anchor bolts with slots on the laboratory floor. In this study, beam ends close to the stubs are referred to as support ends. The stubs were enlarged to facilitate their anchorage with steel corbels of the setup, and the support ends are regarded as fixed ends. The beam ends close to the middle joint are referred to as joint ends. And the middle joint is named as the torsion preventer since it was enlarged to prevent out-of-plane translation and rotation of beams. The torsion preventer was designed to be as wide as the clear distance between two clip beams, thereby constraining the out-of-plane translational movement and the out-of-plane torsion around the longitudinal axis of joint ends. As a result, the displacement of the two-span beam was restricted to the plane formed by the beam-column axes. The column had a cross-sectional dimension of 160 × 160 mm$^2$, with a clear height of 1800 mm. The single beam had a clear span of 1620 mm and a cross-sectional dimension of 140 mm × 200 mm. The size of longitudinal bars was determined based on the principle of equal reinforcement ratios with the prototype structure, and detailed layouts are demonstrated in Table 2 and Fig. 1. In the table, 'T′ and 'R′ denote ribbed and round bars, respectively. The measured compressive strength of concrete cubes with a maximum aggregate size of 19 mm is listed in Table 1, and the measured tensile strength of steel bars is listed in Table 3.

Specimen S1 served for a preliminary test. In the test, 6000 kg of upper loads were applied on the top of torsion preventer, i.e., the top of substructure. Besides, 2520 kg of secondary load boxes were uniformly suspended on beams to simulate uniformly distributed loads. For each beam, half of applied uniformly distributed loads were transferred to the column because two ends of beams were fixed before the column removal. Therefore, the equivalent concentrated load on the top of substructure was calculated as 6000 + 2520/2, which equals 7260 kg. In following tests, these secondary load boxes were canceled to avoid obstructing the view of high-speed cameras and interfering with displacement sensors. Specimen S4 served as the control group for all ICR specimens and was compared with specimen SID, in which the RC column was replaced by a wooden temporary support, representing nominal column removal (NCR). Variables were designed to serve two purposes: firstly, to directly compare the consequence of ICR and NCR, and secondly, to investigate the influence of different impact parameters. In the ICR series, the variables were the upper loads (S1), the elevations of impact points (S2), the cross-sectional area of column longitudinal bars (S3), and the concrete strength (S5), as listed in Table 1. Except for specimen SID, all other specimens, with identical

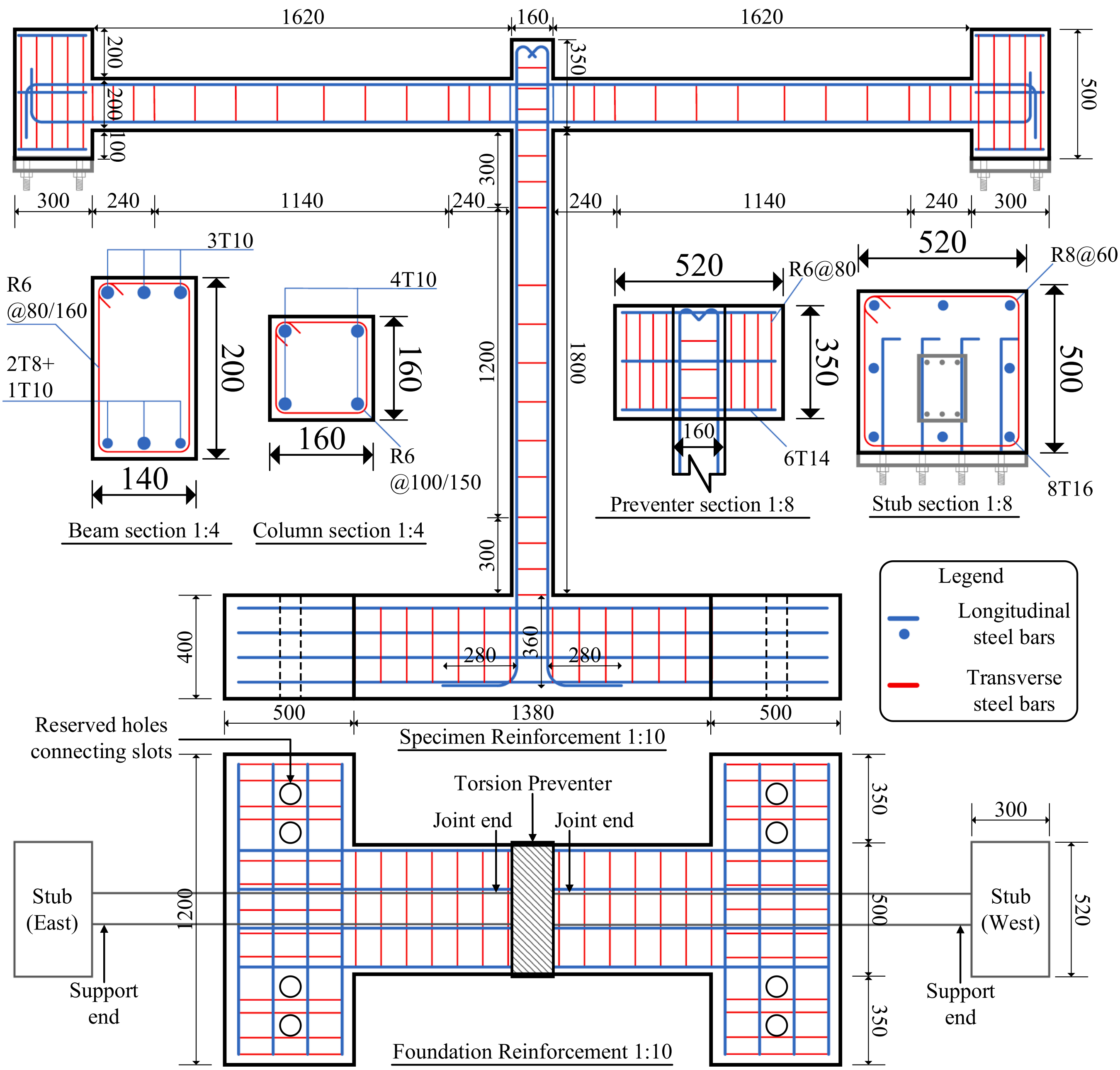


**Fig. 1.** Schematic diagram of the specimen.

**Table 1**
Specimen parameters.

| Specimen | Removal method | Impact location | Column longitudinal bars | Upper loads (kN) | Concrete strength (MPa) |
|---|---|---|---|---|---|
| S1 | Impact | Middle | 4T10 | 63 | 35.4 |
| S2 | Impact | Lower | 4T10 | 33 | 34.7 |
| S3 | Impact | Middle | 4T12 | 33 | 31.9 |
| S4 | Impact | Middle | 4T10 | 33 | 28.9 |
| S5 | Impact | Middle | 4T10 | 33 | 40.1 |
| SID | Nominal | / | / | 33 | 33.0 |

Note: The name SID stands for specimen employing the event-independent assumption.

geometric configurations and dimensions, had columns cast monolithically with the superstructure.

### 2.2. Test setup

This study utilized and adapted the pendulum impact setup in the College of Civil Engineering at Hunan University [24,36]. Fig. 2 shows a schematic diagram and an on-site photo of the setup, where the pendulum consists of a hammer, a load cell, and pendulum weights. To provide sufficient strokes when applying the upper loads, the lever system amplifying loads in the original setup was replaced with a steel-made load box (weighing 363 kg), applying loads with an approximate maximum stroke of 550 mm. The loads were applied in gravitational acceleration during the deformation of substructures, thereby emulating real-world scenarios. Weights were placed inside the load box, of which four corners were constrained in guide rails by ball transfer units. Therefore, the box's movement is restricted to only the

**Table 2**
Reinforcement details.

| | $b$ | $h_0$ | Bars | Reinforcement ratio |
|---|---|---|---|---|
| Beam top longitudinal bars | 140 | 179 | 3T10 | 0.94 % |
| Beam bottom longitudinal bars | 140 | 180 | 2T8 + 1T10 | 0.71 % |
| Column longitudinal bars | 160 | 160 | 4T10/ 4T12 | 1.227 %/1.767 % |
| Critical region stirrups of beams | 140 | - | R6 @ 80 | 0.5048 % |
| Non-critical region stirrups of beams | 140 | - | R6 @ 160 | 0.2524 % |
| Critical region stirrups of columns | 180 | - | R6 @ 100 | 0.3141 % |
| Non-critical region stirrups of columns | 180 | - | R6 @ 150 | 0.2094 % |

Note: $b$ is the width of sections, $h_0$ is the effective height of sections, units are mm, the area transverse reinforcement ratio is selected for stirrups. The S4 specimen employed 4T12 for column bars.

**Table 3**
Measured parameters of steel bars.

| Type and diameter (mm) | R6 | T8 | T10 | T12 |
|---|---|---|---|---|
| Elastic modulus (GPa) | 228 | 211 | 171 | 183 |
| Yield strength (MPa) | 383 | 497 | 476 | 437 |
| Ultimate strength (MPa) | 525 | 644 | 623 | 641 |
| Elongation ratio (%) | 19.6 | 20.8 | 20.7 | 20.3 |

vertical direction.

### 2.3. Loading regime

The conventional low-speed impact loading is employed to simulate vehicular collisions on buildings. The designed impact velocity is 5.7 mm/msec, which, according to similarity laws, corresponds to an impact velocity of approximately 60 km/h in prototype structures. Due to energy losses in mechanical motions and errors in measuring the lifting height, the measured impact velocity, as listed in Table 4, was lower than the designed value. Before the impact tests, the load box was placed on the top of substructures to apply an upper load. In other words, the load box applies compression due to gravity but cannot apply tension and does not contribute inertia to the substructure. Then, the pendulum was lifted by an electric hoist to the predetermined height and then impacted the target column after mechanical detacher released. After column removal tests, static tests were conducted on substructures in which collapse was arrested. Weights in the load box were gradually and slowly increased by 4.2 kN per step until the occurrence of progressive collapse, thereby obtaining the residual load-bearing capacity of substructures.

Both the progressive collapse dynamic test and the impact test are one-off, implying that each test can, in the strict sense, capture only a single point of the structural performance. Therefore, it is necessary to design upper loads to obtain typical dynamic behavior of structures subjected to progressive collapse. Two calculation methods and the finite element (FE) analysis were employed to determine the upper loads. On the one hand, a modified Park-Gamble model [37] and a simplified model of catenary action (CA) resistance [38] were employed to estimate CAA and CA peak resistance, respectively. The calculated CAA peak resistance is 65 kN, corresponding to a column removal point (CRP) displacement of 29 mm, and the calculated CA peak resistance is 71 kN, corresponding to a CRP displacement of 360 mm. On the other hand, a multi-linear model [39] was employed to calculate critical points of load-displacement curves. Additionally, a static load-displacement curve was obtained through a FE model simulating the pseudo-static loading condition. Load-displacement curves of the two-span beam obtained by the FE and the multi-linear models are illustrated in Fig. 3. Both models exhibited consistent trends in the CAA stage, which indicates that the setup provide relatively strong restraints since it was explicitly modeled and predicted comparable resistance to the multi-linear model with strong lateral stiffness conditions. The multi-linear model predicted a higher peak resistance in the CA stage than the FE model. To observe the dynamic progressive collapse process of RC frame structures, the upper loads applied in specimen S1 were approximately equal to the calculated peak resistance of CA. For investigating the inertial effects of downward force exerted by lateral failures of the column and for reserving bearing capacity for subsequent

**Table 4**
Impact parameters of specimens.

| Specimen | Impact velocity (mm/msec) | Impact mass (kg) |
|---|---|---|
| S1 | 5.67 | 2217 |
| S2 | 5.34 | 2217 |
| S3 | 5.64 | 2217 |
| S4 | 5.22 | 2217 |
| S5 | 5.66 | 2217 |

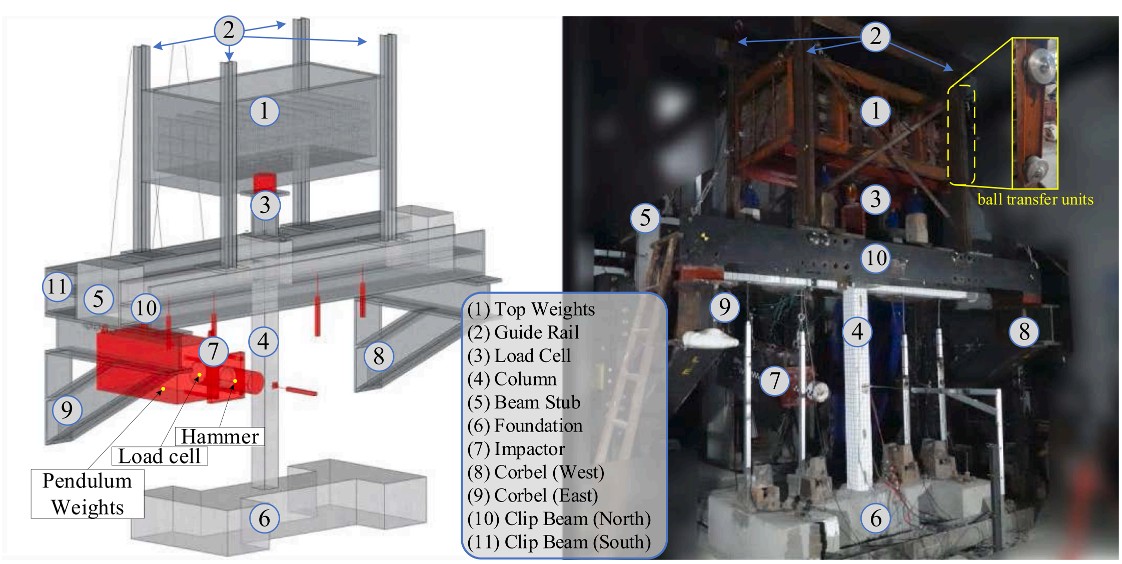


**Fig. 2.** Test setup and the specimen.

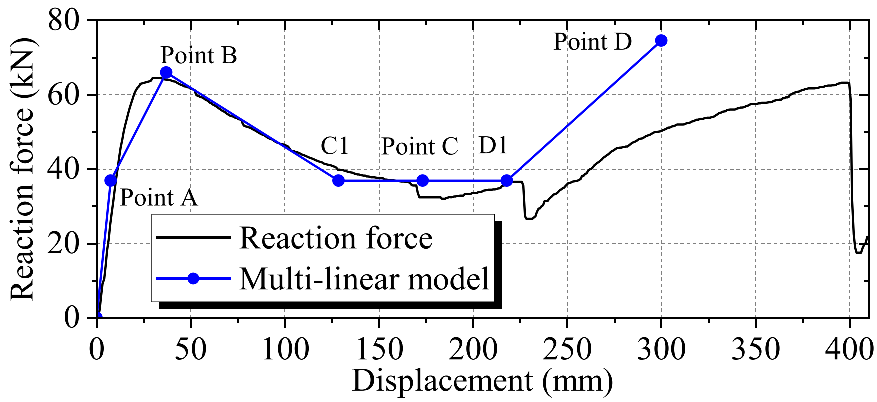


**Fig. 3.** The displacement vs. load curve obtained by the FEM simulation and multi-linear model.

residual bearing capacity tests, the upper loads applied for specimens SID and S2-S5 were 33 kN.

### *2.4. Instrumentations*

Two high-speed cameras were employed to record the testing process. One camera recorded the overall conditions at a frame rate of 1981 Hz, while the other captured the details of the impacted column at a frame rate of 2000 Hz. A load cell, labelled LA, was installed on the top of substructure to measure the upper load, and another load cell, labelled LI, situated between the hammer and the pendulum weights to measure the impact force.

Fig. 4 illustrates the sensor scheme of the experiment, in which sensors were symmetrically arranged. Strain gauges were installed on selected points of longitudinal bars in beams and columns to measure their axial strain. The names of strain gauges follow the Beam/Point/Elevation/Location naming rule. For example, WST1 stands for the west beam, side measurement point, top layer bar, and the T1 location, as shown in Fig. 4. Linear displacement sensors were positioned under the bottom of beams at equal intervals of 540 mm to record the vertical displacement of beam segments. The spatial requirements necessitated by the pendulum movement and the deformed column rendered linear displacement sensors ineffective for directly measuring the CRP displacement. Therefore, an indirect measurement scheme was employed during the tests. Tracking targets were positioned at specific measurement points, and CRP displacement was tracked and calculated using high-speed videos, which were processed through the Tracker software.

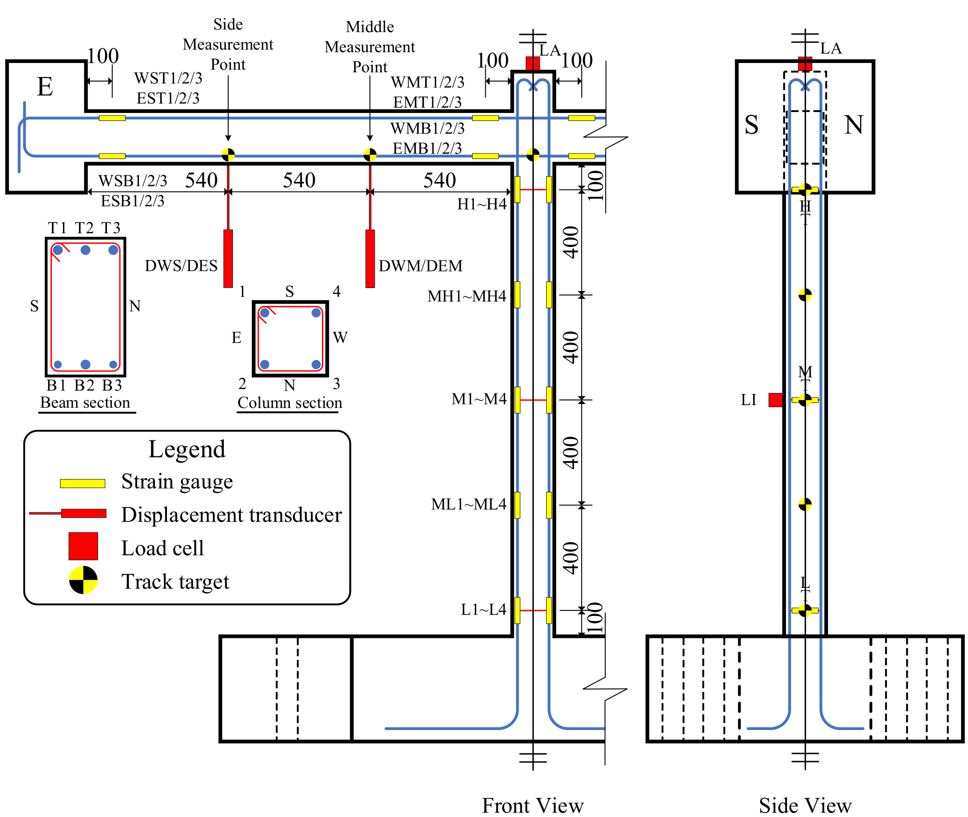


**Fig. 4.** Locations of instrumentation and strain gauges.

## 3. Experimental results

### 3.1. Damage modes

#### 3.1.1. During the impact

High-speed videos were utilized to observe the damage conditions during the impact process. Fig. 5 illustrates the damage process of specimen S4 in details. The initiation moment of contact between the pendulum and column is denoted as 0 msec. At 9 msec, straight cracks formed on the back side of impact, and crushing appeared on the impact-facing side, indicating the early formation of damage around the impact point. By 21 msec, significant straight cracks had developed around the impact point, and the column approached the flexural failure. At 90 msec, the termination of impact loading stage was signified by fractures of all four longitudinal bars at the column base end. At 143 msec, two longitudinal bars on the back side of impact and around the impact point were observed fractured. Then both the column and the pendulum continued their motion due to inertia, but the column no longer exerted downward force on the superstructure. At this point, the CRP vertical displacement of the two-span beam continued to develop, reaching its maximum value at approximately 565 msec.

Based on above observations, the impact process could be characterized with four typical moments, as illustrated in Fig. 6 for remaining specimens. T0 represents the initiation of impact; T1 is the moment when indications of damage appear on RC columns; T2 is the moment when the downward force terminates; and T3 is the moment when the CRP displacement reaches its maximum value. For the specimen S1, T3 is marked by the failure of the CA. The side view of the specimen S1 was obstructed by the secondary load boxes, and the side impact process for the specimen S3 was not captured. Therefore, front view images are displayed for the two specimens in Fig. 6. The column in specimen S1 primarily exhibited flexural failure, but a shear plug was also observed. Specimen S2 subjected to low-elevation impact exhibited shear failure. Additionally, the T2 moment for specimens S2 and S3 occurred later than for specimens S4 and S5. Intervals between T0 and T2 for specimens S1, S4, and S5 was approximately 100 msec, whereas for specimens S2 and S3, they were around 150 msec. Intervals between T2 and T3 was approximately 250 msec for specimens S2 and S3, whereas for specimens S4 and S5, they reached 450 msec. Reasons for these differences are specifically analyzed in Section 3.2.

#### 3.1.2. After the impact

After impact loading, specimen S1 collapsed. Specimens S2 to S5 exhibited significant plastic deformation of beams but refrained collapse. The specimen SID employing NCR did not show noticeable deformation. Fig. 7 illustrates the crack distributions of two-span beams. In this figure, all ICR specimens exhibited significant crack damage at both the joint and support ends, which is generally positively correlated with the CRP displacement, as seen from the curves in Section 3.2. Among them, specimen S1 showed the most severe cracks and concrete damage, with large areas of concrete spalling at ends, which could be ascribed to the severe beam deformation and CA failure. Besides, ICR specimens generally displayed varying degrees of concrete crushing at the upper parts of joint ends.

Fig. 8 illustrates damaged columns after ICR. It can be observed that the concrete at the impact point was completely crushed, even leading to cross-sectional concrete voids. At the impact point or column ends, fractured longitudinal bars exhibited typical necking indicating tensile failures. Therefore, the vertical load-bearing capacity of impacted columns had been lost, and the termination of downward force process owes to complete fractures of longitudinal bars at any section of the column or exhaustion of impact kinetic energy. For specimen S1, all longitudinal bars fractured at the impact point. For specimens S4 and S5, all longitudinal bars fractured at the base end. In contrast, for specimens S2 and S3, complete fractures did not appear on any single section.

### 3.2. Displacement responses

#### 3.2.1. Column displacement

The lateral displacement of impacted columns, as presented in Fig. 9, are represented by time-history curves of tracking targets on the hammer because their movement is associated in the impact loading

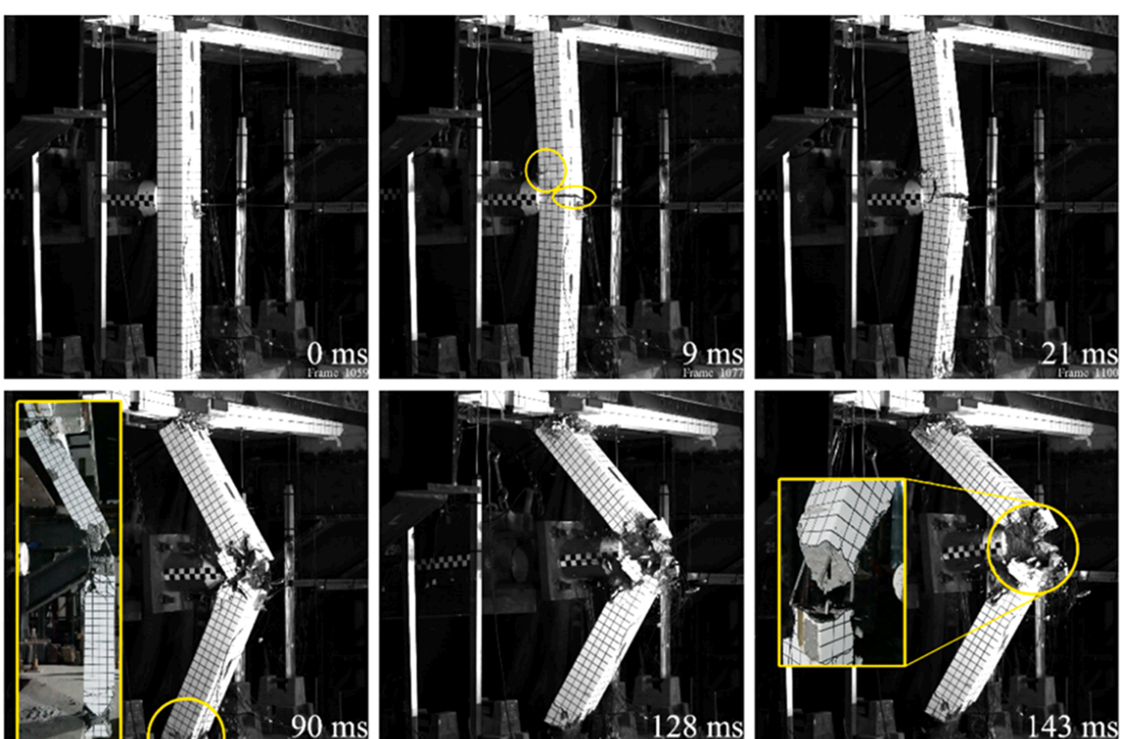


**Fig. 5.** Side impact damage process of S4.

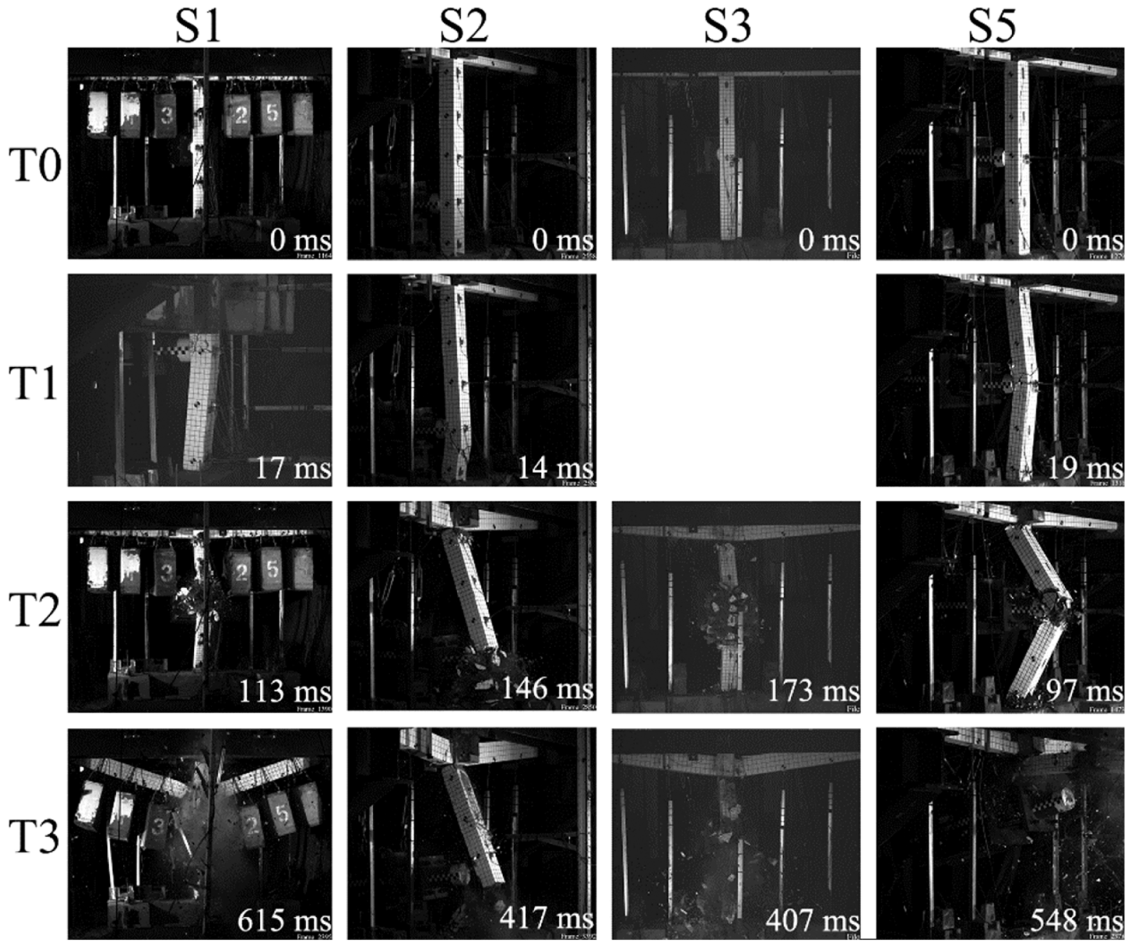


**Fig. 6.** Typical moment of damaged specimens.

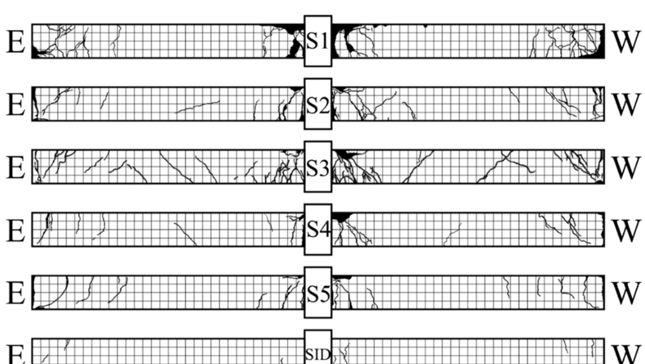


**Fig. 7.** Crack distributions of two-span beams.

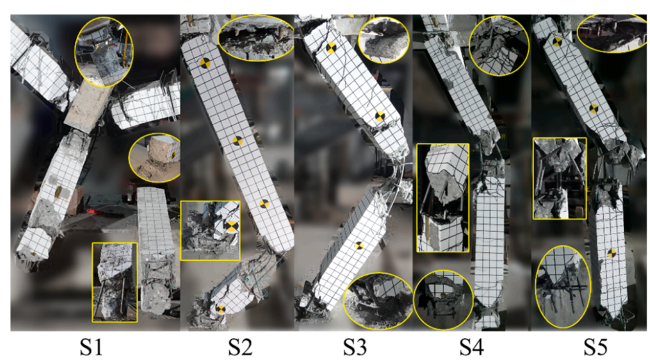


**Fig. 8.** Damage conditions of impacted columns.

stage. And in this figure, the straight line with a slope of designed velocity 5.70 mm/msec is included for reference. In this figure, specimens S1, S4, and S5, in which the impact points located at the middle height of columns, exhibited relatively consistent velocity trends. The velocity of specimens exhibited a certain degree of attenuation for gradually deviating from the reference line. Hence, some kinetic energy of the pendulum was consumed in the ICR process, but remaining kinetic energy is still sufficient to drive the pendulum's movement. The velocity of specimen S2 attenuated more rapidly. This is likely due to the low-elevation impact, which results in a different energy dissipation mechanism compared to other specimens.

#### 3.2.2. Beam displacement

Fig. 10 compares the vertical displacement of beam segments measured by displacement sensors. The vertical displacement is generally symmetrical since values and trends on mirrored locations are similar. For ICR specimens, the displacement increased upwardly due to arching effects induced by impact loading, with an average displacement of 4.98 mm. Then, it rapidly declined and reached the first peak at the T2 moment, which is defined in Fig. 6. After the disappearance of downward force, the displacement temporarily increased due to restored elastic potential energy in beams, followed by the second decline till the substructure attained static equilibrium or collapse. The NCR specimen also exhibited minor arching effects when the temporary support removed, with an upward displacement of 0.3 mm. On all ICR

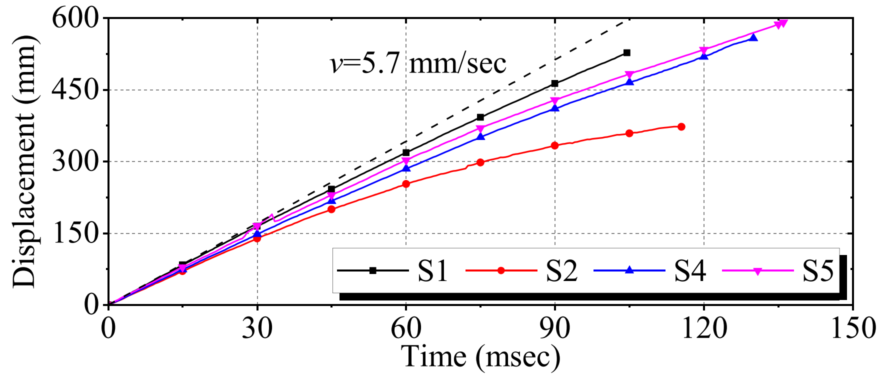


**Fig. 9.** Lateral displacement histories at impacted points.

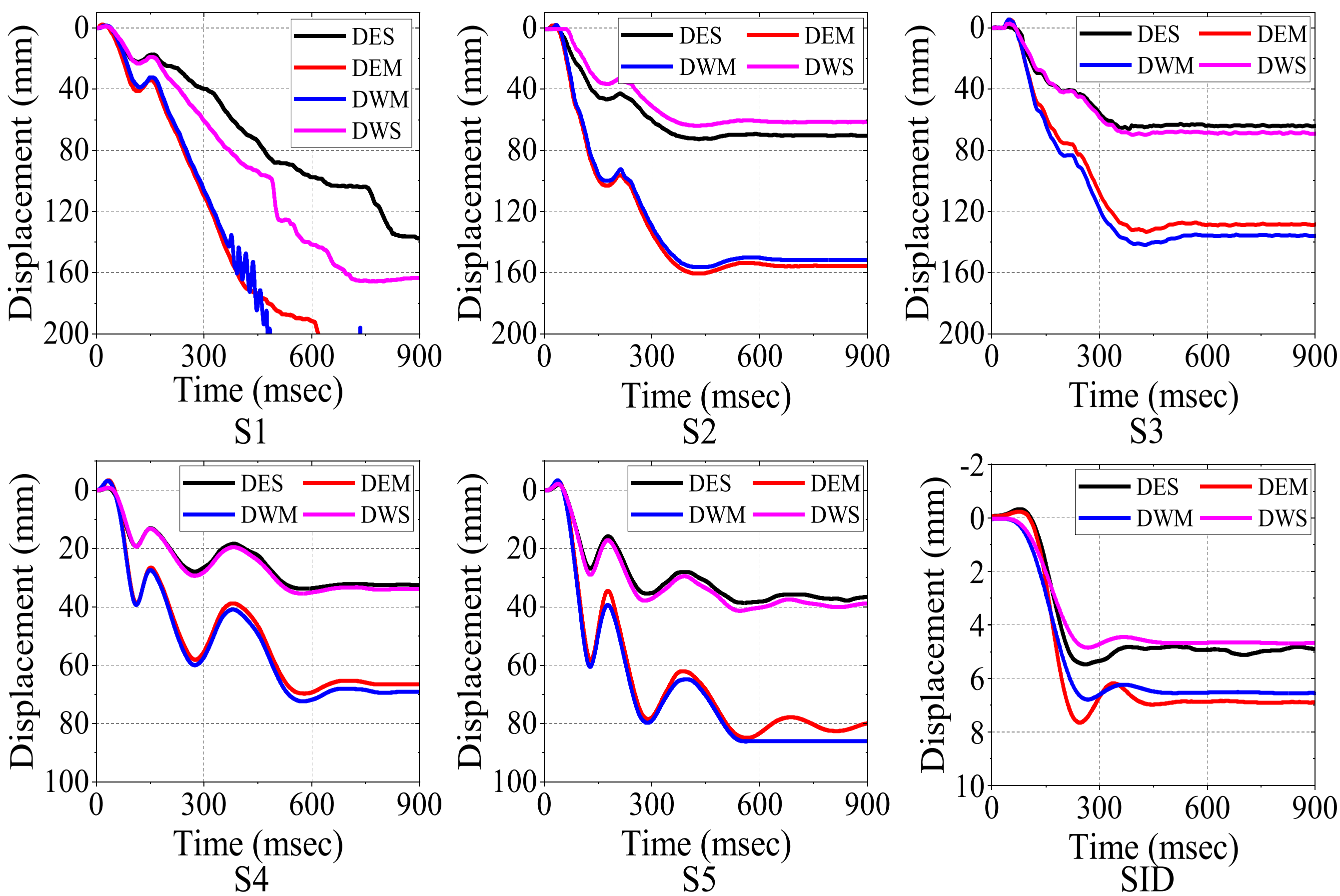


**Fig. 10.** Displacement histories of measuring points on beams.

specimens, two critical peaks appeared on the displacement history. The first peak corresponds to the T2 moment, which occurred when all column longitudinal bars fractured at the impact point section (S2) or base end section (S4 and S5), or upon the exhaustion of impact kinetic energy. At this moment, the upper loads, freely falling with gravitational acceleration, had not yet reached the top of substructures, so the CRP displacement partially recovered. Then, the upper loads reached the top and caused further deformation till the second peak. In contrast, the dynamic process of the NCR specimen was relatively straightforward. Following column removal, the substructure directly attained a new static equilibrium state under the upper loads.

At CRPs, the vertical displacement was indirectly measured by high-speed video tracking. To validate the precision of the method, the video-tracked and sensor-measured displacement of four randomly selected measurement points across different specimens are compared in Fig. 11, in which the '-trk' suffix denotes data from video tracking. The results indicate a high degree of consistency between two methods. Fig. 12 compares the CRP displacement of all specimens. As illustrated, the displacement at T3 for ICR specimens, which is denoted as D3, is significantly greater than that for NCR. Specifically, D3 for specimens S2 to S5 were 221 mm, 213 mm, 107 mm, and 126 mm, respectively, whereas specimen SID showed a displacement of 7.2 mm. The curves of S4 and S5 specimens fluctuated more rapidly because columns fractured at the base and remaining parts rotated around the top joint under the push of pendulum, leading to eventual collisions. Notably, before the T2 moment, the curves of ICR specimens were all below the free fall curve,

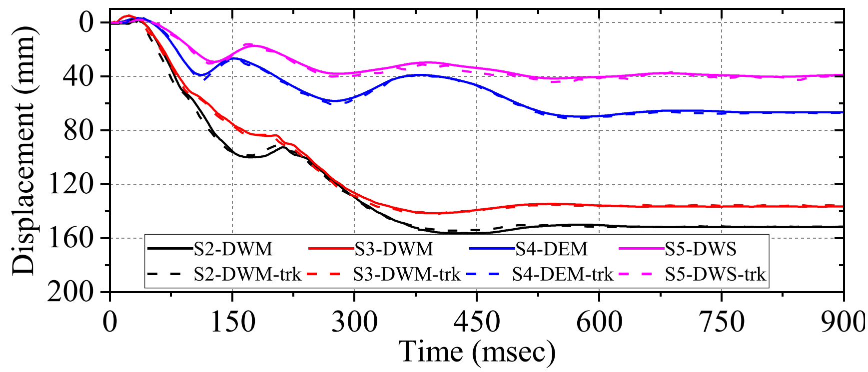


**Fig. 11.** The displacement comparison between transducer and video tracks.

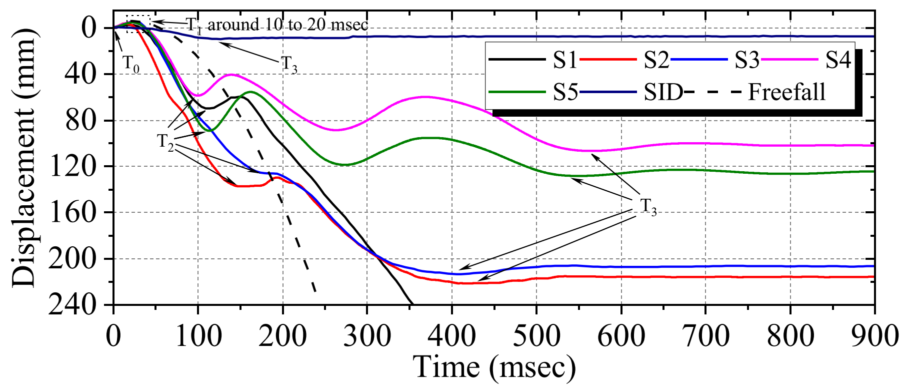


**Fig. 12.** The vertical displacement history of CRPs.

**Table 5**
Displacement details of specimens.

| Specimen | S-T3 | M-T3 | CRP-T2 ($D_2$) | CRP-T3 ($D_3$) | ($D_3$-$D_2$)/ $D_3$ |
|---|---|---|---|---|---|
| S2 | 66 | 154 | 137 | 221 | 0.38 |
| S3 | 67 | 132 | 126 | 213 | 0.41 |
| S4 | 33 | 68 | 59 | 107 | 0.45 |
| S5 | 33 | 83 | 89 | 126 | 0.29 |
| SID | 4.68 | 6.72 | - | 7.2 | - |

Note: ‘S’ and ‘M’ denote measurement points on beams near the support and middle joint end, respectively. The S-T3 displacement is the average of DWS and DES at T3. The M-T3 displacement is the average of DWM and DEM at T3.

consistent with the predictions made in the reference [21] and indicating the existence of downward force. More detailed displacement data are summarized in Table 5.

### 3.3. Strain responses

#### 3.3.1. Strains of impacted columns

The strain time-history curves of the longitudinal bars at the High (H) and Low (L) planes in the impacted column of specimen S4 are illustrated in Fig. 13. Measurement points near the impact-facing side, i.e., H1/H4 and L1/L4, underwent rapid tension after impact initiated, and L1/L4 failed at approximately 10 msec, probably because strain gauges at these points were being out of range. H1 and H4 reached peak tensile strains around 25 msec and then failed, while tensile strains began to increase in L2 and L3. Similarly, strains in H2 and H3 began to increase around 41 msec. Therefore, it can be anticipated that after bars near the impact-facing side failed, bars near the opposite side exerted the downward force. As the impact loading continued, strains in H2 and H3 continued to increase and stabilized around 90 msec, while strains in L2 and L3 lost signal between 60 to 80 msec. RC column in specimen S4

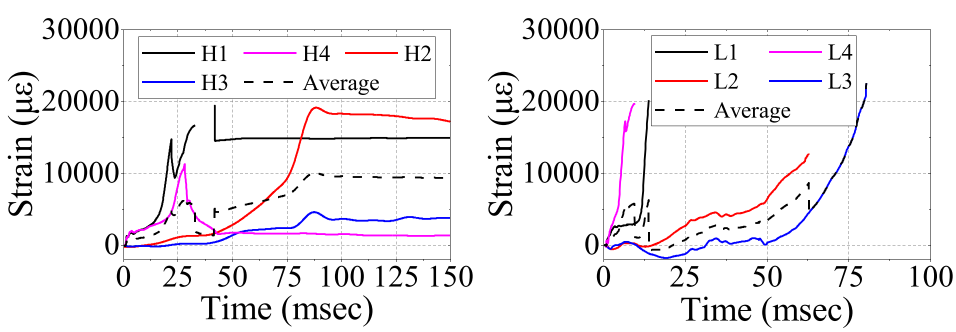


**Fig. 13.** Column longitudinal bar strain histories of specimen S4.

fractured from its foundation at 90 msec, suggesting stabilized strains in H2 and H3 after 90 msec due to fractured bottom bars, altering the boundary condition. Subsequent loading did not increase strains or induce downward force.

#### 3.3.2. Beam strain comparisons

The influence of column removal methods is also revealed through the comparison of beam longitudinal bar strains. Fig. 14 and Fig. 15 display the strain time-history of beam longitudinal bars for the specimen SID and specimen S4, respectively, where positive values indicate tension and negative values indicate compression. For the specimen SID, the strain at symmetrical points was similar, and strain gauges generally continued to function after column removal. The strain stabilized at around 600 msec, which aligns with the time required for displacement stabilization. At this moment, the top longitudinal bars at the support ends were under tension, while the bottom bars were under compression. At the joint ends, the top bars were under compression, and the bottom bars were under tension. Most measurement points remained within the elastic range, with only the points at the joint ends reaching yielding. Considering that the specimen SID only exhibited minor flexural cracks and a CRP displacement of only 7.2 mm, it can be inferred that the specimen was transitioning from the flexural action to the CAA.

It can be observed from Fig. 15 that strains in specimen S4 were significantly higher than specimen SID, with most gauges failed due to being out of range after impact. Considerably high strains were detected on the top bars of support ends and bottom bars of joint ends. After the impact, the bottom longitudinal bars at the support ends remained under compression with strains approaching or exceeding the yield point: average microstrain (με) was −1158 for ESB1 and ESB3, and −2428 for WSB2 and WSB3. At the joint ends of the east beam, two top bars were in tension (EMT1 and EMT3), with a strain sum of 1132, indicating tension at the measurement point. There was significant variation in strains at the top bars of joint ends of the west beam, with an average compressive με of −3750 for WMT2 and WMT3, and a tension με of 150 for WMT1. Current mainstream theories for progressive collapse resistance typically argue that the longitudinal bars at beam ends are in a yielding state during the CAA. From Fig. 15, it can be observed that all sections exhibited strains that failed in tension, suggesting the yielding of both top bars at support ends and the bottom bars at joint ends. Additionally, the compression strains of the west beam at the support and joint ends both exceeded −2000, indicating compression yielding at these sections. With a CRP displacement of 107 mm, approximately 0.53 times the beam height, it could be inferred that specimen S4 was transitioning from the CAA to the CA when it reached static equilibrium.

### 3.4. Force responses

Fig. 16 presents the impact force time-history measured by the load cell LI for specimens S1 to S5. The curves reveal two distinct phases: the first phase corresponds to the initial peak impact force, lasting roughly 2 msec demonstrated in the Fig. 16 (f). The peak impact forces for most specimens are around 340 kN, with S2 exhibiting the highest peak at 446 kN. The second phase is the plateau phase, where the impact forces are smaller, with a maximum of only 130 kN in S3. During the plateau phase following column removal, contact forces exist because the pendulum continued to drive the RC column's movement, but their interaction no longer induced a downward force on the superstructure. A FE analysis was performed to estimate the lateral static bearing capacity of columns. The results indicated that the maximum bearing capacity was 98.9 kN for columns with 4T10 longitudinal bars and loaded at the mid-height. When the loading location is the low-elevation point, and when equipping 4T12 longitudinal bars and loading at the mid-height, the maximum bearing capacity was 164 kN and 131 kN, respectively. It can be concluded that although the capacity was higher under the latter two conditions, larger areas of longitudinal bars barely influenced the peak impact force. Low-elevation impact increased both

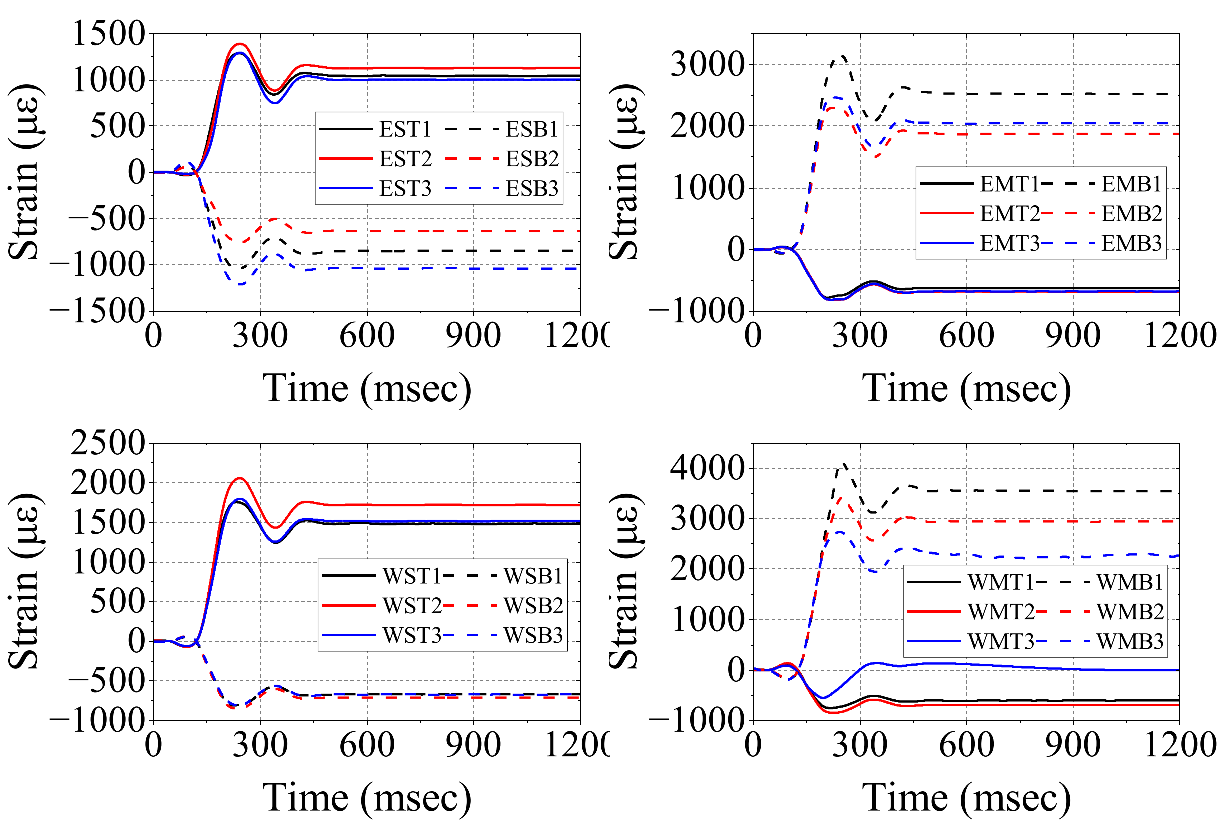


**Fig. 14.** Beam longitudinal bars strain histories of the specimen SID.

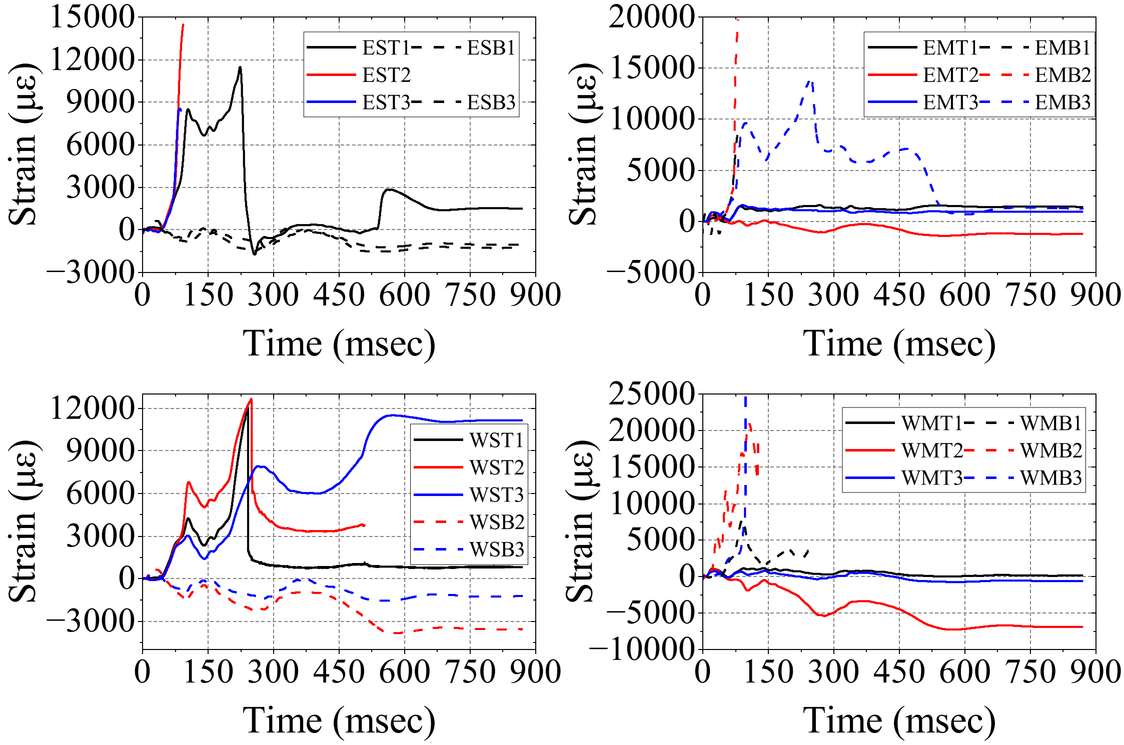

**Fig. 15.** Beam longitudinal bar strain histories of the specimen S4.

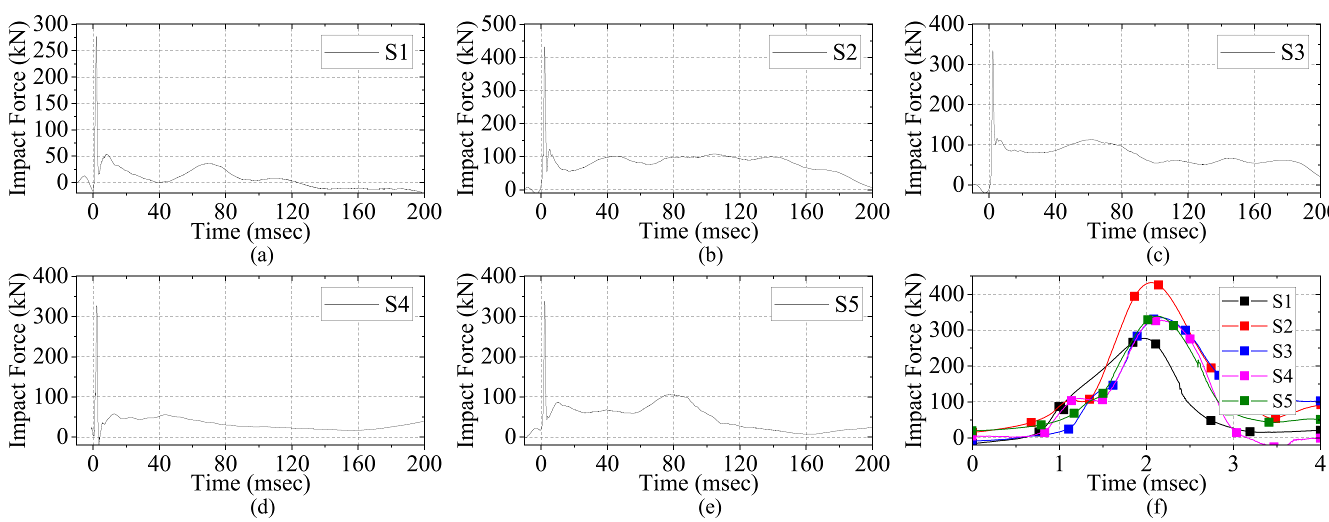

**Fig. 16.** Impact force histories of ICR specimens.

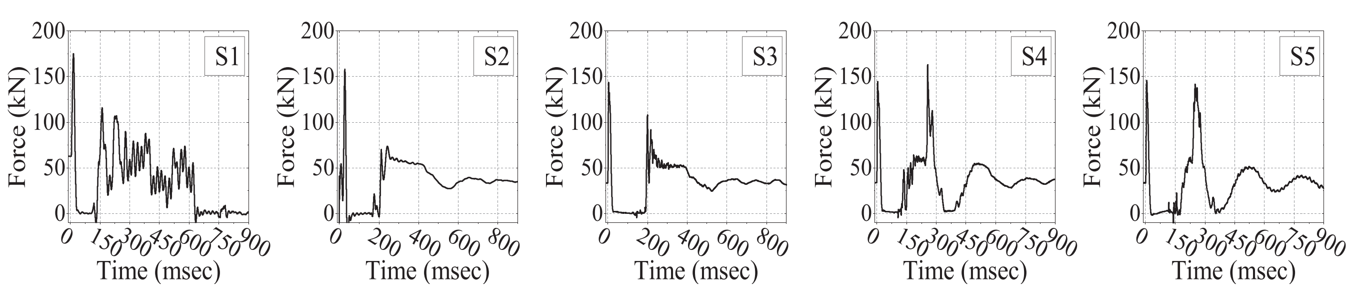

**Fig. 17.** Upper loads histories of ICR specimens.

the static capacity and the peak impact force.

Fig. 17 demonstrates the upper load curves of ICR specimens measured by the load cell LA. These curves correlate with the vertical displacement curves of CRPs (Fig. 12) and damage process (Fig. 6). All upper load curves exhibit a sharp increase after impact initiation, reaching a peak force of approximately 150 kN, corresponding to arching effects shown in the Fig. 10. At this point, the load box exhibited a trend of upward movement, combined with compression and inertial effects on the load cell, and resulted in peaks in the load curves. Subsequently, all curves dropped back to near zero, coinciding with the CRP displacement curves falling below the free fall curve. During the stage, the CRP underwent acceleration greater than gravitational acceleration and caused the short free fall of the upper load box and load cell. The curves then rose again, occurring at approximately 150 msec for specimens S1, S4, and S5, and around 200 msec for S2 and S3. This corresponds to the second decline in the CRP displacement curve, as shown in Fig. 12. For specimen S1, the upper load curve dropped back to zero again around 620 msec, closely aligning with the failure of CA (615 msec), as shown in Fig. 6, and suggesting simultaneous free fall of the load box, load cell, and CRP after the substructure collapsed.

### *3.5. Static residual bearing capacity*

Static tests were conducted on specimens S2 to S5 and SID to evaluate their residual bearing capacity. The actual approach was to further pile weights, 4.2 kN per step, in the top load box until the failure of mechanisms resisting progressive collapse. Fig. 18 demonstrates the load-displacement curves measured during the static residual bearing capacity tests, where the solid lines represent steps in which substructures can maintain static equilibrium, and dashed lines denote the last load step at which collapse occurred. When applying the last step of loads, all specimens, except for specimen S2, did not immediately collapse, but the deformation developed at rapid rates. The sudden collapse commonly happens within 1 min after applying the last step of loads. In specimen S2, the substructure collapsed upon the operating technician, weighing around 80 kg, standing on the load box to release the connection between the weight and the loosened steel rope of the crane 10 to 20 s after the step_4 load was applied. The specimen SID exhibited the highest residual bearing capacity since it kept stable when extra loads reached 21 kN. Specimens S2, S3, and S4 could only bear 12.6 kN of extra loads, while the value for specimen S5 was 16.8 kN. Therefore, taking the residual bearing capacity of SID as the baseline, specimens S2 to S4 lost 40 % of residual bearing capacity, while the specimen S5 lost 20 %. Besides, during the static tests, deformation development was not obvious in any specimen. The displacement increments were 7, 8, 15, and 20 mm for specimens S2 to S5, before they collapsed, and 14.1 mm for specimen SID. The above results indicate that differences exist in terms of residual bearing capacity for substructures subjected to ICR and NCR, and the approach of applying static loads by gravity loading could directly influence the obtained progressive collapse resistance of structures.

The performance point of specimen SID after NCR is positioned before the peak resistance of CAA. In the static test, the increased loads move the performance point toward the peak resistance of CAA. Once the loads surpass the peak, the substructure can only provide comparable resistance at the CA stage. The area under the resistance curve with respect to the abscissa axis physically represents the work done by the resistance, and it is equivalent to the mechanical energy dissipated by the substructure to reach the corresponding displacement. On the other hand, since the applied gravity load is constant and displacement-independent, the substructure must fully dissipate the gravitational potential energy to reach a new static equilibrium position. In this substructure, the work done by the resistance in the CA stage is less than the undissipated gravitational potential energy, leading to the failure of specimen SID to resist progressive collapse after surpassing the peak resistance of CAA.

For ICR specimens, the CRP displacement during the impact loading stage has already exceeded the displacement corresponding to the peak resistance of CAA due to the downward force. After the downward force disappears, the elastic potential energy restored in substructures causes a brief increase in the CRP displacement (Fig. 12). Subsequently, the upper load recontacts the top of substructure, and the gravity loading stage begins. The load applied during the stage, due to the kinetic energy transformed from the free-fall process, requires consideration of dynamic effects. As the kinetic energy is dissipated, the performance point eventually falls below the resistance curve, resulting in a significant CRP vertical displacement. In static tests, the increased gravity load causes the CRP displacement to continue increasing along the resistance curve and leads to substructure collapse as the gravity load exceeds the CA resistance. Similar to the specimen SID, the ICR substructures need to find a new performance point satisfying static equilibrium during the CA stage and meet the energy balance requirement; otherwise, substructures will collapse.

Results and analysis from the above tests indicate that the energy equilibrium condition also needs to be considered for maintaining static equilibrium in static tests applying gravity loads. Due to the 'valley' that typically exists between the CAA peak resistance and the CA peak resistance, structures might directly collapse once the loads exceed the CAA peak resistance, even if higher resistance can be provided during the CA stage. It is well-recognized that using displacement-controlled actuators for loading can obtain a complete resistance curve, which is useful for determining whether the structure can meet the energy equilibrium condition. However, to capture the actual anti-collapse behavior of structures, force-controlled gravity loading should be employed. In large-scale progressive collapse tests that closely approximate the scale of actual buildings [16, 40–42], gravity loading is also

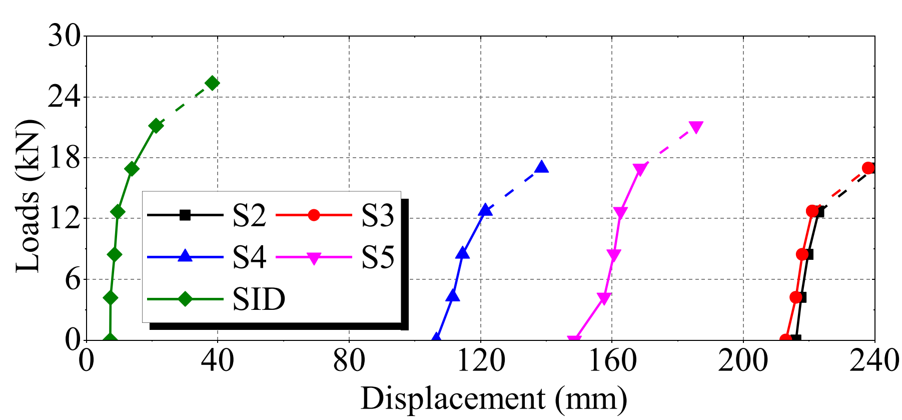


**Fig. 18.** The comparison of static residual bearing capacity.

the only feasible approach.

It should be noted that the CAA peak resistance obtained from the calculation method and FE model is approximately 65 kN, while the maximum gravity load applied to specimen SID was 58.2 kN, comprising 33 kN from the top load box and 25.2 kN added in the static test of residual bearing capacity. There are several potential reasons accounting for differences between the actual bearing capacity of substructures and the calculated value. For instance, despite weights being slowly placed with utmost efforts in the static test, small dynamic disturbances were unavoidable; boundary conditions of the two-span beams assumed in the calculation method were too idealized; and concrete creep under high-stress conditions and the plastic flow of steel bars could also be influential. Similar deferred collapse phenomenon under sustained gravity loads has also been reported in previous progressive collapse tests [16, 43]. Excluding seismic-induced collapses, gravity loads typically dominate the forces acting on structures undergoing progressive collapse. This phenomenon partly explains catastrophic incidents such as the collapses of Rana Plaza and Champlain Towers South [44], which resulted in significant casualties. Although cracks and other warning signs appeared in these structures before the collapse, they were not subjected to extreme events. If the static deformation before member failures is insufficient to alert occupants to evacuate in time, it can result in significant casualties.

## 4. Parametric study

Comparisons of experimental results in the previous section indicate that ICR caused more severe damage to substructures than NCR. The downward force generated during the failure process of columns leads to significant influence on substructures, in which higher CRP displacement and lower residual bearing capacity are exhibited. Based on these facts, the influence of different impact parameters on the progressive collapse performance are further compared and discussed in this section.

The main difference between specimens S2 and S4 is the elevation of impact points. In specimen S4, the impact point is located at the middle of the column, 900 mm above the column bottom, while in specimen S2, it is 450 mm above the column bottom. Fig. 19 (a) demonstrates the situations of these two RC columns during and after the failures. Different impact elevations resulted in different initial failure modes: specimen S2 exhibited diagonal cracks, while the primary cracks in specimen S4 were parallel to the impact direction. After the impact, the concrete near the impact points of both specimens was completely crushed, and the columns entirely lost their vertical load-bearing capacity, as can be seen in Fig. 19 (a). It is worth noting that the bottom end of column longitudinal bars in specimen S2 did not fracture, but, at the top end, the two longitudinal bars near the impact-facing side fractured (see Fig. 8).

The results presented in Fig. 12 and Table 5 indicate that both the displacement at the termination of downward force, corresponding to the T2 moment, and the maximum CRP displacement, corresponding to the T3 moment, are greater for specimen S2 than for S4. Considering that the concrete strength for specimen S2 (34.7 MPa) is slightly higher than for S4 (28.9 MPa), this indicates that a low-elevation impact causes more severe damage to the substructure than an impact at the middle-height. In terms of test results, the T2 moment (146 msec) in specimen S2 is later than specimen S4 (90 msec), resulting in a longer duration of downward force for S4. In terms of failure mechanisms, the later T2 moment for specimen S2 is related to the failure mode of the concrete at column ends. This phenomenon can be explained by Fig. 19 (b) and (c), in which the concrete in specimen S2 exhibited extensive cracking and spalling because the column bottom end near the impact point. Therefore, a relatively long length of debonded longitudinal bars entered the plastic flow state at the bottom end. At the top end, only a straight principal crack developed, so the plastic deformation of longitudinal bars concentrated in a relatively short length, resulting in bar fractures prior to the bottom end. In specimen S4, the locations of plastic deformation were symmetrical about the impact point, so failure modes at both ends were similar to the top end of specimen S2. Before the column lost vertical load-bearing capacity, considerable concentrated plastic hinges appeared at the middle-height of the column and both ends. Therefore, longitudinal bars near the impact-facing side at both ends will fracture when the rotation angle of column is small. At this point, only the two longitudinal bars near the back side of impact can bear the downward force, and they will also soon fracture under the remaining impact energy, leading to the disappearance of the downward force.

Specimens S3 and S4 employed 4T12 and 4T10 for longitudinal bars, respectively, with cross-sectional areas of 452 $mm^2$ and 314 $mm^2$. Theoretically, specimen S3 has the potential of generating greater downward force on the superstructure. Fig. 12 confirms this guess, with the displacement of specimen S3 reaching 213 mm, which is 1.99 times that of S4, when they reattained static equilibrium. Fig. 20 compares the strain in longitudinal bars at the high (H) and low (L) measurement points of the RC columns for the two specimens. The strain variation trends for both are generally similar, with strain gauges on longitudinal bars near the impact-facing side first failing in tension. The characteristic of specimen S3 is that, after the longitudinal bars near the impact-

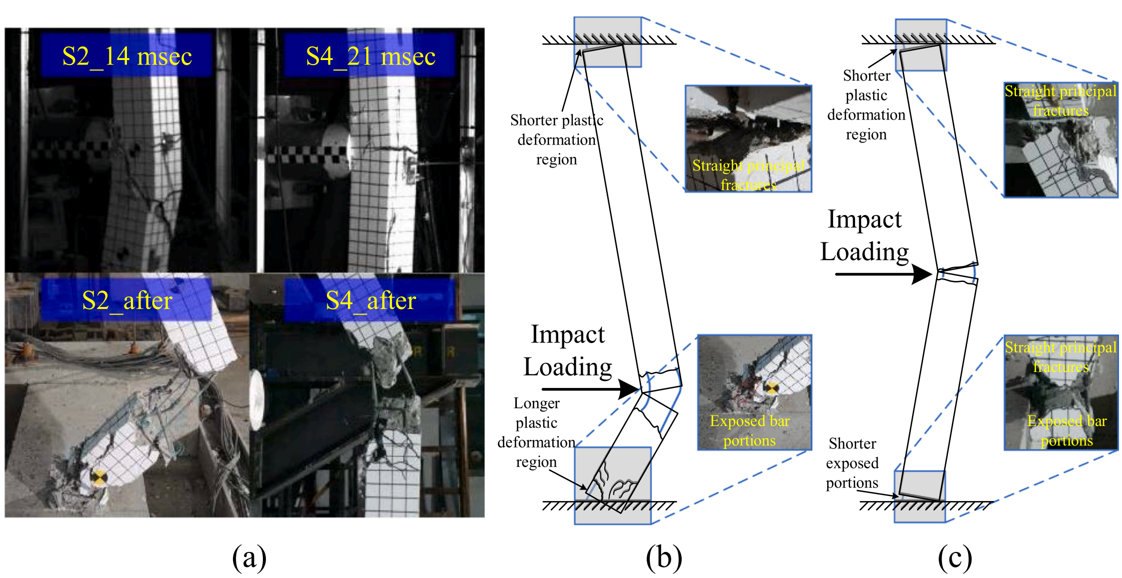


**Fig. 19.** S2 and S4 comparison: (a) impact point details, (b) specimen S2, (c) specimen S4.

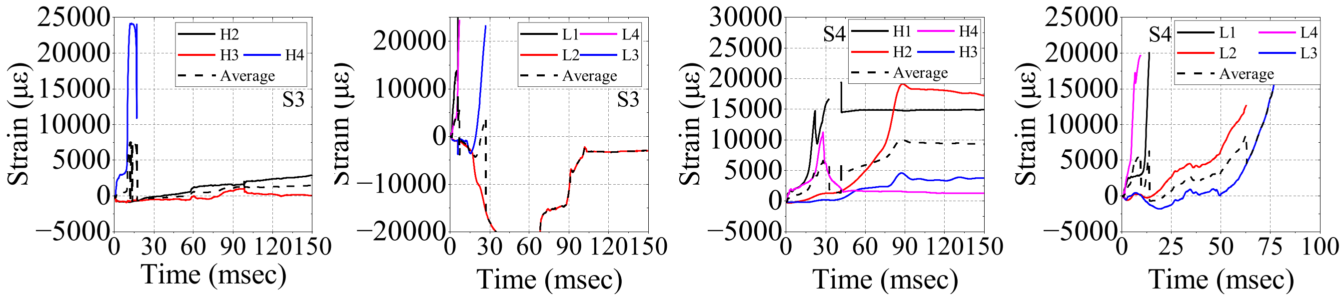


**Fig. 20.** The comparison of column strain histories between S3 and S4.

facing side fractured, the impact energy was insufficient to continue fracturing the bars near the back side of impact. Consequently, the strain gauges did not fail even when the tensile strain in H2 and H3 increased. At the low measurement point, the tensile strain in L3 rapidly increased after L1 and L4 fractured. Meanwhile, the L2 remained in compression although its compressive strain continuously decreased. Its tensile strain eventually stabilized around −3000. The strain response of specimen S4 has been described in Section 3.3.2 and mainly involved the rapid successive fractures of the longitudinal bars on both the impact-facing side and back side at the bottom end, leading to the disappearance of the downward force. The experimental results indicate that more energy is consumed for fracturing the RC column longitudinal bars if the bar diameter is increased. Consequently, the fixed boundary conditions at both ends of the impacted column are less likely to be damaged, so the impact-induced downward force process is extended, causing more significant substructure damage.

The primary difference between specimens S5 and S4 is the concrete strength, which is 40.1 MPa and 28.9 MPa, respectively. As illustrated by Fig. 12, the displacement curve of specimen S5 essentially overlaps with those of other substructures before the T2 moment. Fig. 8 shows that specimens S5 and S4 both exhibited concrete voids around the impact point and bar fractures near the back side of impact. These mediocre results suggest that concrete strength has no significant influence on the progressive collapse resistance of substructures during the impact loading stage. Responses in this stage primarily depend on the duration of the downward force, and more fundamentally, on the failure modes of impacted columns. Similar to specimen S4, the longitudinal bars at the bottom column end of specimen S5 exhibited significant necking (Fig. 8), indicating the complete fracture at this location and the subsequent disappearance of downward force.

However, Table 5 suggests that specimen S5 exhibited the smallest

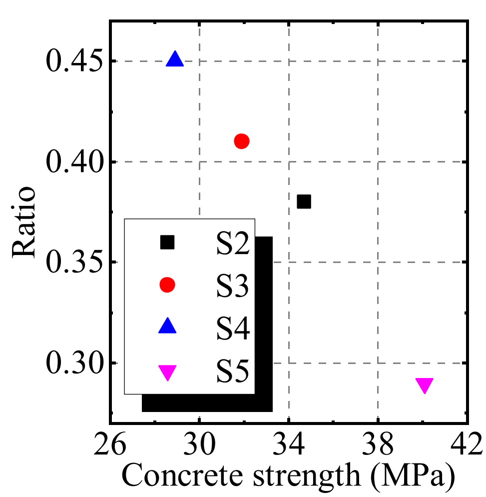


**Fig. 21.** Concrete strength and the gravity stage displacement vs. total displacement ratio.

vertical displacement of 37 mm developed during the gravity loading stage. Also, it had the smallest ratio of vertical displacement developed during the gravity loading stage to the total vertical displacement, at 0.29. This ratio is above 0.38 for specimens S2 to S4 and shows a linear relationship with concrete strength, as illustrated in Fig. 21, suggesting that higher concrete strength may help reduce deformation under this stage. Additionally, Fig. 18 indicates that higher concrete strength contributes to improved residual load-bearing capacity because only specimen S5 refrained collapse under the fourth level of additional load (16.8 kN) among ICR specimens. The premise for a structure to avoid progressive collapse after column removal is that the dissipated energy must exceed the gravitational potential energy of the applied gravity load [45]. Therefore, higher concrete strength might imply that less deformation is required to dissipate the same amount of energy, thereby enhancing the performance of the specimen during the gravity loading stage and in residual load-bearing capacity tests.

## 5. Simplified calculation of downward pulling forces

The downward force resulted in significantly higher displacement in ICR specimens. Therefore, the quantification of downward force is a promising work; once accomplished, impact loading could be incorporated into existing event-independent design frameworks of progressive collapse. In a previous study [21], the authors constructed a dynamic model of the phenomenon, in which the influence of downward force on structures was simplified as an analysis of SDOF system, as depicted in Fig. 22. In this diagram, $\Delta_{st}$ and $\Delta_{pf}$ denote the vertical displacement of CRP under NCR and additional vertical displacement due to downward force, respectively. Under the circumstance, the mass point satisfies the following dynamic equilibrium equation:

$$M_e\ddot{x} + K_B x = P + M_e g \tag{1}$$

where, $M_e$ is the equivalent mass of CRP, $K_B$ is the stiffness of the two-span beam, $x$ is the CRP displacement, $\ddot{x}$ is its acceleration, $g$ is the gravitational acceleration, $P_{pf}$ is the downward force. According to Eq. (1), the downward force can be expressed as:

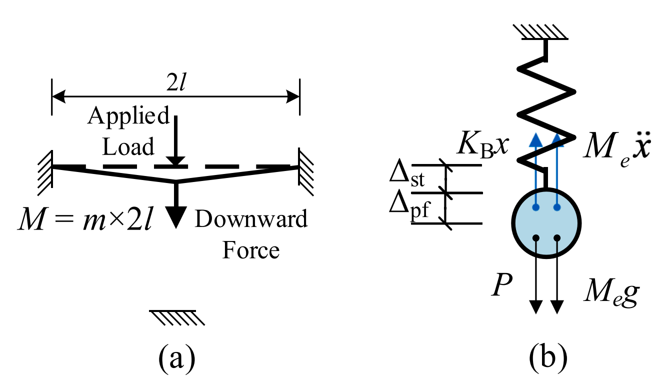


**Fig. 22.** The analytical model downward force.

$$P_{pf} = M_e(\ddot{x} - g) + K_B x \quad (2)$$

So, the downward force is composed of two components satisfying linear superpositions. One is the inertial force that needs to be overcame when accelerating the equivalent mass of CRPs. This component represents the dynamic effects, referred to the downward force resisting inertia. The equivalent mass is determined based on the principle that its kinetic energy is equal to that of the two-span beam, i.e.,

$$M_e = M_c + 2\int_0^l m\phi^2(x)\mathrm{d}x \quad (3)$$

where, $M_c$ is the concentrated mass of the torsion preventer, $m$ is the mass per unit length of the beam, $\phi(x)$ represents the shape function of the two-span beam. Shape functions of two-span beams under concentrated loads are commonly the straight-type[46]. The displacement data presented in Table 5 corroborates this finding, demonstrating that the displacement at S-points and M-points were approximately proportional to their respective distances from the support ends. Therefore, it can be concluded that the shape function $\phi(x) = x/l$. By substituting specimen parameters into Eq. (3), $M_e$ can be determined as 171 kg, in which the $M_c$ is 99 kg according to specimen dimensions and material density.

During the impact loading stage, the CRP acceleration exceeds gravitational acceleration, so the deformation in this stage is not caused by upper loads. $K_B x$ represents the restoring force that needs to be overcame to induce deformation at the CRP. This force is also part of the downward force affected by the boundary conditions provided by the two-span beam, referred to the downward force resisting deformation. It is equivalent to the progressive collapse resistance of the two-span beam considering static concentrated load at the CRP. In summary, if the acceleration during the ICR process at the CRP and the static progressive collapse resistance of structures are obtained, the downward force can be calculated using Eq. (2).

However, the solutions of Eq. (2) would be very sophisticated, even if mathematical expressions of $\ddot{x}$ and $K_B$ were obtained, because it is a second-order ordinary differential equation with variable coefficients. Therefore, this method adopts certain simplifications for evaluations of the downward force. One of the considerations is to replace the time-varying acceleration with an average acceleration. According to the differential equation of motion, displacement increments of a mass point with zero initial velocity are proportional to their acceleration over the period. In the experiment, the maximum average acceleration $23.35\ \mathrm{mm/msec^2}$ was found on the specimen S5, corresponding to a downward force resisting inertia of 3.99 kN. On the other hand, the peak resistances of CAA and CA are approximately 65 kN and 71 kN, respectively, according to theoretical models mentioned in section 2.3. So, the downward force resisting inertia does not play a dominant role. It should be noted that downward force resisting inertia may be comparable or even dominant in other scenarios, such as the high-velocity impact or explosion. The simplification is limited to scenarios similar to this study, in which low-velocity impact and relatively small equivalent mass of CRPs are considered.

The downward force resisting deformation can be expressed by incorporating the multi-linear model in Section 2.3. The experimental results suggest that the downward force is observed when the CRP displacement is about 100 mm, at which point the dominant action is transitioning from CAA to CA. Therefore, only the first increase portion of the CA stage in the model is calculated. Fig. 23 illustrates the downward force-displacement curve represented using specimen S4 and processed according to above considerations and Appendix. B. In the figure, the downward force terminates when the full-section longitudinal bar fracture occurs, with the peak downward force being 68.99 kN, which is the sum of the force resisting inertia (3.99 kN) and the peak force resisting deformation (65 kN). In specimen S4, the CRP displacement was 59 mm when the downward force ended. Hence, the downward force relating to the CRP displacement can be expressed as:

$$P(d) = \begin{cases} \dfrac{P_A - P_0}{d_A}d + P_0 & d \le d_A \\ \dfrac{P_B - P_A}{d_B - d_A}d + \quad P_A - \dfrac{P_B - P_A}{d_B - d_A}d_A & d_A < d \le d_B \\ \dfrac{P_{C1} - P_B}{d_{C1} - d_B}d + P_B - \dfrac{P_{C1} - P_B}{d_{C1} - d_B}d_B & d_B < d \le d_{C1} \\ P_{C1} & d_{C1} < d \end{cases} \quad (4)$$

where, $P(d)$ represents the downward force exerted on the CRP corresponding to a vertical displacement $d$. $P_0$ is the initial downward force regardless of CRP displacement, i.e., the downward force component resisting inertia. $P_A$, $P_B$, and $P_{C1}$ denotes downward forces corresponding to critical points on the load-displacement curves obtained from the multi-linear model [39]. $d_A$, $d_B$, and $d_{C1}$ denote CRP displacements of these critical points. Specifically, point A refers to the transition in structural behavior when longitudinal bars begin to yield; Point B refers to the CAA peak resistance; and point C signifies the cease of CAA and the onset of CA, according to Fig. 3, Fig. 23, and reference [39].

It should be noted that the multi-linear model cannot account for downward force terminations. Therefore, in Fig. 23, the downward force is stipulated to disappear when the CRP displacement exceeds the defined termination point. The termination point displacement of specimen S4 is less than the displacement of point C1. Thus, the curve beyond the termination point is drawn with a dashed line to indicate the potential of this method to consider downward force over a wider displacement range. Admittedly, the termination point displacement is determined by experimental data, and the inherent relationship between termination point displacement, specimen parameters, and impact conditions requires further investigations.

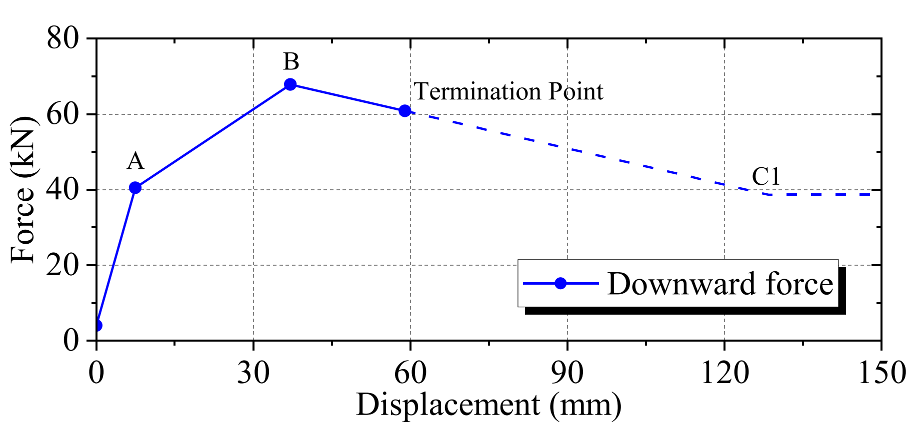


**Fig. 23.** The displacement vs. downward force curve of the specimen S4.

## 6. Conclusions

This study performed the progressive collapse experiment of RC frame structures employing impact loading as trigger events for the first time. The findings are offered as a reference for subsequent event-dependent studies, which could further explore some limitations in this study such as lack of slab effects, lack of spatial effects, and limited impact angles. Also, it was found that the prototype structure designed based on Chinese codes does not completely satisfy provisions in some other codes, such as ACI 318–19 [47]. Nevertheless, current experimental results essentially revealed discrepancies between ICR and NCR. The effects of impact elevations, cross-sectional areas of column longitudinal bars, and concrete strength on the progressive collapse behavior under ICR were examined. The results basically confirm the fact that the downward force exerted during the impact loading stage aggravates the risk of progressive collapse and causes the reduction of residual load-bearing capacity. The event-independent assumption significantly overestimates the collapse resistance of RC frame structures. Detailed conclusions are as follows:

(1) Due to the longitudinal bars connecting the column and superstructure, the downward force exerted during the impact loading stage induced an initial displacement that exceeded the displacement corresponding to CAA peak resistance. All five impacted columns exhibited concrete crushing around impact points, and in some cases, longitudinal bars fractured either at the impact point or the base end. In contrast, the substructure with NCR experienced only a simple dynamic process to re-establish static equilibrium, without exceeding the CAA peak resistance.
(2) Before the termination of downward force, CRP displacement curves of ICR specimens were below the free-fall curve, indicating the influence of downward force. The curve of the NCR specimen remained above the free-fall curve. The downward force caused significant differences in CRP displacement, ranging from 107 to 221 mm for ICR specimens, significantly greater than the NCR specimen. ICR specimens exhibited pronounced crack development and plastic hinge rotations at beam ends. Conversely, the NCR specimen exhibited only minor flexural cracks on the tensile side of beam ends.
(3) Compared to the NCR specimen, the reduction of residual bearing capacity due to ICR was between 20 % to 40 %. This difference is attributed to the downward force causing two-span beams to exceed the CAA peak resistance, and this fact is not considered in the event-independent assumption. Furthermore, the NCR specimen exhibited immediate collapse after surpassing the CAA peak resistance. This collapse occurred because the gravitational potential energy that need to be dissipated during the descent to the new static equilibrium exceeded the substructure's energy dissipation capacity. This highlights the influence of load application methods on energy balance considerations in progressive collapse scenarios.
(4) The parameter study indicates that low-elevation impact and larger cross-sectional areas of column longitudinal bars are adverse for maintaining progressive collapse resistance of structures under ICR. This is evidenced by obviously larger CRP displacement compared to the control group. The direct cause is the later fracture of longitudinal bars in the impact loading phase. The underlying impact mechanisms relating concrete damage patterns require further investigation. Higher concrete strength does not significantly improve structural performance during impact loading, but it can alleviate the reduction of progressive collapse resistance and of residual bearing capacity during gravity loading.
(5) Based on SDOF models, the simplified calculation method of downward force is proposed. The downward force consists of a component that resists the inertia of superstructures, representing dynamic effects, and a component that resists the deformation of superstructures, representing the boundary conditions. The component resisting deformation is predominant in low-velocity impact scenarios. In this study, the peak downward force was 68.99 kN.
(6) Due to the nascent stage of relevant research issues, the influence of specific factors like actual vehicle collisions, impact velocity, impact mass, and locations of impact column removal still requires further investigation. Moreover, the findings suggest the necessity of studying the interaction between column members and frame structures subjected to impact loading.

### CRediT authorship contribution statement

**Qing-Feng He:** Project administration. **Wang-Xi Zhang:** Visualization. **Yun Zhou:** Funding acquisition. **Jing-Ming Sun:** Resources. **Wei-Jian Yi:** Supervision, Conceptualization. **Fan Yi:** Investigation, Formal analysis.

### Declaration of Generative AI and AI-assisted technologies in the writing process

During the preparation of this work the authors used ChatGPT-4o in order to check the objective correctness of the language, such as whether a noun is countable or noncountable. After using this tool, the authors reviewed and edited the content as needed and take full responsibility for the content of the publication.

### Declaration of Competing Interest

The authors declared that they have no conflicts of interest to this work.

### Data availability

Data will be made available on request.

### Acknowledgements

The authors sincerely appreciate the funding support provided by the National Natural Science Foundation of China (NSFC) (No. 51878264, No. 52278306, No. 52078201), the Department of Science of Technology of Hunan Province (No. 2022SK2096), the Natural Science Foundation of Hunan Province of China (No. 2023JJ70003) and the Hydraulic Science of Technology Project of the Hunan Provincial Department of Water Resources (No. XSKJ2023059-31).

## Appendix A. Supplementary material

The high-speed videos of impact tests are archived at https://drive.google.com/drive/folders/1VqdVLitelBClO9-LesoKyZxpligKuMPz?usp=drive_link.

## Appendix B. Calculations of downward forces resisting inertia

The values determining the average acceleration and the downward force resisting inertia in Section 5 are presented in this appendix. According to displacement curves illustrated in Fig. 12, critical displacement data of each ICR specimen are given in Table A1.

**Table A1**
Time and displacement data during the impact loading stage.

| Specimen | $T_{ad}$ (msec) | $D_{ad}$ (mm) | $T_2$ (msec) | $D_2$ (mm) | $D_{ff}$ (mm) | $A_a$ (mm/msec2) | $M_e$ (kg) | $P_{pfi}$ (kN) |
|---|---|---|---|---|---|---|---|---|
| S1 | 19 | −2.7 | 114 | 70 | 44 | 6.24 | 171 | 1.07 |
| S2 | 13 | −4.1 | 157 | 137 | 102 | 3.79 | 171 | 0.65 |
| S3 | 22 | −6.9 | 178 | 126 | 119 | 1.11 | 171 | 0.19 |
| S4 | 21 | −4.9 | 100 | 59 | 31 | 10.54 | 171 | 1.80 |
| S5 | 25 | −6.8 | 105 | 89 | 28 | 23.35 | 171 | 3.99 |

Note: $T_{ad}$ is the time CRP reaching the highest displacement due to arching effects since impact initiates, and $D_{ad}$ is the corresponding highest displacement. $D_2$ is the displacement corresponding to $T_2$, which denotes the time the downward force terminates. $D_{ff}$ is the calculated free-falling displacement between $T_{ad}$ and $T_2$, assuming zero vertical velocity at $T_{ad}$. $A_a$ is the average acceleration deducting the gravitational acceleration. $P_{pfi}$ is the downward force resisting inertia calculated by $M_e$ and $A_a$.

In the table, $T_{ad}$, $D_{ad}$, $T_2$, and $D_2$ are obtained from tests. Derivative data are calculated as follow:

$$D_{ff} = \frac{1}{2}g(T_2 - T_{ad})^2 \tag{A.1}$$

$$A_a = g\left(\frac{D_2 - D_{ad}}{D_{ff}} - 1\right) \tag{A.2}$$

$$P_{pfi} = M_e A_a \tag{A.3}$$

Based on Table A1, it can be concluded that the highest $A_a$ appears on specimen S5. Corresponding $P_{pfi}$ is determined according to (A.3) as follows: $P_{pfi} = M_e A_a = 171 \times 23.35 = 3.99$ kN.

## References


[1] Adam JM, Parisi F, Sagaseta J, Lu X. Research and practice on progressive collapse and robustness of building structures in the 21st century. Eng Struct 2018;173:122–49.
[2] Code for design of concrete structures. Beijing: Ministry of Housing and Urban-Rural Development of the People's Republic of China,; 2010.
[3] (DoD) DoD. UFC 4–023-03: Design of buildings to resist progressive collapse. Washington, DC, USA; 2009.
[4] (GSA) GSA. Alternate path analysis & design guidelines for progressive collapse resistance. Washington, DC; 2013.
[5] Shi Y, Li Z-X, Hao H. A new method for progressive collapse analysis of RC frames under blast loading. Eng Struct 2010;32:1691–703.
[6] Elsanadedy HM, Almusallam TH, Alharbi YR, Al-Salloum YA, Abbas H. Progressive collapse potential of a typical steel building due to blast attacks. J Constr Steel Res 2014;101:143–57.
[7] Gombeda MJ, Naito CJ, Quiel SE, Fallon CT. Blast-induced damage mapping framework for use in threat-dependent progressive collapse assessment of building frames. J Perform Constr Fac 2017;31:04016089.
[8] Kiakojouri F, Sheidaii MR, De Biagi V, Chiaia B. Blast-induced progressive collapse of steel moment-resisting frames: numerical studies and a framework for updating the alternate load path method. Eng Struct 2021;242:112541.
[9] Gernay T, Gamba A. Progressive collapse triggered by fire induced column loss: detrimental effect of thermal forces. Eng Struct 2018;172:483–96.
[10] Li Z, Liu Y, Huo J, Rong H, Chen J, Elghazouli AY. Experimental assessment of fire-exposed RC beam-column connections with varying reinforcement development lengths subjected to column removal. Fire Saf J 2018;99:38–48.
[11] Stewart MG. Spatial variability of explosive blast loading and its effect on damage risks to reinforced concrete buildings. Eng Struct 2023;285.
[12] Yu J, Rinder T, Stolz A, Tan K-H, Riedel W. Dynamic progressive collapse of an RC assemblage induced by contact detonation. J Struct Eng 2014;140.
[13] Shi YC, Jiang R, Li ZX, Ding Y. A substructure based method for damage assessment of RC frame structures under close-in explosion. Eng Struct 2022;272.
[14] Kang H, Kim J. Progressive collapse of steel moment frames subjected to vehicle impact. J Perform Constr Fac 2015;29:04014172.
[15] Janfada IS, Sheidaii MR, Kiakojouri F. Comparative analysis of code-based dynamic column removal and impact-induced progressive collapse in steel moment-resisting frames. Int J Steel Struct 2023;23:1576–86.
[16] Xiao Y, Kunnath S, Li FW, Zhao YB, Lew HS, Bao Y. Collapse test of three-story half-scale reinforced concrete frame building. Acids Struct J 2015;112.
[17] Qian K, Li B. Quantification of slab influences on the dynamic performance of RC frames against progressive collapse. J Perform Constr Fac 2013;29:04014029.
[18] Yin XJ, Zhang B, Yu QQ, Gu XL. Overturning collapse responses of RC frame-shear wall structures induced by failure of vertical members. Eng Struct 2023;285.
[19] Sun JS, Jia YS, Yao YK, Xie XQ. Experimental investigation of stress transients of blasted RC columns in the blasting demolition of buildings. Eng Struct 2020;210.
[20] Li ZX, Liu HK, Shi YC, Ding Y, Zhang HS. Experimental investigation on dynamic response behavior of PC beam-column sub-assemblages under middle-joint drop-weight loading. J Build Eng 2023;80.
[21] Yi F, Yi W-J, Sun J-M, Ni J, He Q-F, Zhou Y. On the progressive collapse performance of RC frame structures under impact column removal. Eng Struct 2024;307:117926.
[22] Sharma H, Hurlebaus S, Gardoni P. Performance-based response evaluation of reinforced concrete columns subject to vehicle impact. Int J Impact Eng 2012;43:52–62.
[23] Liu B, Fan W, Guo W, Chen B, Liu R. Experimental investigation and improved FE modeling of axially-loaded circular RC columns under lateral impact loading. Eng Struct 2017;152:619–42.
[24] Sun J-M, Yi W-J, Chen H, Peng F, Zhou Y, Zhang W-X. Dynamic responses of RC columns under axial load and lateral impact. J Struct Eng 2023;149:04022210.
[25] Gurbuz T, Ilki A, Thambiratnam DP, Perera N. Low-elevation impact tests of axially loaded reinforced concrete columns. Acids Struct J 2019;116.
[26] Remennikov A., Kaewunruen S. Impact resistance of reinforced concrete columns: experimental studies and design considerations; 2006.
[27] Huynh L, Foster S, Valipour H, Randall R. High strength and reactive powder concrete columns subjected to impact: Experimental investigation. Constr Build Mater 2015;78:153–71.
[28] Fan W, Xu X, Zhang Z, Shao X. Performance and sensitivity analysis of UHPFRC-strengthened bridge columns subjected to vehicle collisions. Eng Struct 2018;173:251–68.
[29] Zhu X, Zhang Q, Zhang DJ, Du YF, Zhang Q. Experimental and numerical study on the dynamic response of steel-reinforced concrete composite members under lateral impact. Thin Walled Struct 2021;169.
[30] Xian W, Chen WS, Hao H, Wang WD. Experimental and numerical studies on square steel-reinforced concrete-filled steel tubular (SRCFST) members subjected to lateral impact. Thin Walled Struct 2021;160.
[31] Yi W-J, He Q-F, Xiao Y, Kunnath SK. Experimental study on progressive collapse-resistant behavior of reinforced concrete frame structures. Acids Struct J 2008;105:433.
[32] Su Y, Tian Y, Song X. Progressive collapse resistance of axially-restrained frame beams. ACI Struct J 2009;106.
[33] Qian K, Li B. Slab effects on response of reinforced concrete substructures after loss of corner column. Acids Struct J 2012.
[34] Qian K, Li B. Dynamic performance of RC beam-column substructures under the scenario of the loss of a corner column - experimental results. Eng Struct 2012;42:154–67.
[35] Qian K, Li B. Dynamic and residual behavior of reinforced concrete floors following instantaneous removal of a column. Eng Struct 2017;148:175–84.

[36] Sun J-M, Chen H, Yi F, Ding Y-B, Zhou Y, He Q-F, et al. Experimental and numerical study on influence of impact mass and velocity on failure mode of RC columns under lateral impact. Eng Struct 2024;314:118416.
[37] Lu X, Lin K, Li C, Li Y. New analytical calculation models for compressive arch action in reinforced concrete structures. Eng Struct 2018;168:721–35.
[38] Jian H, Zheng Y. Simplified models of progressive collapse response and progressive collapse-resisting capacity curve of RC beam-column substructures. J Perform Constr Fac 2014;28:04014008.
[39] Pham AT, Tan KH. A simplified model of catenary action in reinforced concrete frames under axially restrained conditions. Mag Concr Res 2017;69:1115–34.
[40] Adam JM, Buitrago M, Bertolesi E, Sagaseta J, Moragues JJ. Dynamic performance of a real-scale reinforced concrete building test under a corner-column failure scenario. Eng Struct 2020;210:110414.
[41] Buitrago M, Bertolesi E, Sagaseta J, Calderón PA, Adam JM. Robustness of RC building structures with infill masonry walls: tests on a purpose-built structure. Eng Struct 2021;226:111384.
[42] Makoond N, Setiawan A, Buitrago M, Adam JM. Arresting failure propagation in buildings through collapse isolation. Nature 2024;629:592–6.
[43] Zhou Y, Hu X, Pei Y, Hwang H-J, Chen T, Yi W, et al. Dynamic load test on progressive collapse resistance of fully assembled precast concrete frame structures. Eng Struct 2020;214:110675.
[44] Pellecchia C, Cardoni A, Cimellaro GP, Domaneschi M, Ansari F, Khalil AA. Progressive collapse analysis of the champlain towers South in surfside, Florida. J Struct Eng 2024;150.
[45] Izzuddin BA, Vlassis AG, Elghazouli AY, Nethercot DA. Progressive collapse of multi-storey buildings due to sudden column loss - part I: simplified assessment framework. Eng Struct 2008;30:1308–18.
[46] Li Y, Lu X, Guan H, Ye L. Progressive collapse resistance demand of reinforced concrete frames under catenary mechanism. Acids Struct J 2014;111.
[47] Institute A.C. Building code requirements for structural concrete (ACI 318–19): an ACI standard; commentary on building code requirements for structural concrete (ACI 318R-19): American Concrete Institute; 2019.